

OPEN ACCESS

Organic Solvent-Based Li–Air Batteries with Cotton and Charcoal Cathode

To cite this article: Lajos Nagy *et al* 2024 *J. Electrochem. Soc.* **171** 040509

View the [article online](#) for updates and enhancements.

You may also like

- [Vertically aligned carbon nanotube arrays as thermal interface material for vibrational structure of piezoelectric transformer](#)
Lie Chen, Bin Ju, Zhihua Feng et al.
- [The effects of non-solvent on surface morphology and hydrophobicity of dip-coated polypropylene membrane](#)
Nurul Faiqotul Himma, Anita Kusuma Wardani and I Gede Wenten
- [Capacitive performance of carbon-based supercapacitors using sulfonated poly\(ether ether ketone\) membranes as separators: influences of casting solvents](#)
Guoqiang Li, Na Liang, Jing Xu et al.



Your Lab in a Box!

The PAT-Tester-i-16: All you need for Battery Material Testing.

- ✓ All-in-One Solution with integrated Temperature Chamber!
- ✓ Cableless Connection for Battery Test Cells!
- ✓ Fully featured Multichannel Potentiostat / Galvanostat / EIS!

www.el-cell.com +49 40 79012-734 sales@el-cell.com

EL-CELL[®]
electrochemical test equipment





Organic Solvent-Based Li–Air Batteries with Cotton and Charcoal Cathode

Lajos Nagy,¹ Haymana Serra Üneri,¹ Marcell Árpád Kordován,¹ Tibor Nagy,¹ Ákos Kuki,¹ Dávid Nyul,^{1,2} Petra Pál,³ Zoltán Erdélyi,³ Miklós Zsuga,¹ and Sándor Kéki^{1,2} 

¹Department of Applied Chemistry, Faculty of Science and Technology, University of Debrecen, Egyetem tér 1, H-4032 Debrecen, Hungary

²Doctoral School of Chemistry, University of Debrecen, Egyetem tér 1, H-4032 Debrecen, Hungary

³Department of Solid State Physics, Faculty of Sciences and Technology, University of Debrecen, PO Box 400, H-4002 Debrecen, Hungary

We report on the construction and investigation of Li–air batteries consisting of a charcoal cathode and cotton texture soaked with different organic solvents containing a lithium triflate (LiOTf) electrolyte. Charcoal was found to be an appropriate cathode for Li–air batteries. Furthermore, cycling tests showed stable operation at over 800 cycles when dimethyl sulfoxide (DMSO) and diethylene glycol dimethyl ether (DEGME) were used as solvents, whereas low electrochemical stability was observed when propylene carbonate was used. The charging, discharging, and long-term discharging steps were mathematically modeled. Electrochemical impedance spectroscopy showed Gerischer impedance, suggesting intensive oxygen transport at the surface of the charcoal cathode. Diffusion, charge transfer, and solid electrolyte interphase processes were identified using distribution of relaxation time analysis. In the polypropylene (PP) membrane soaked with LiOTf in DEGME, three different states of Li ions were identified by ⁷Li-triple-quantum time proportional phase increment nuclear magnetic resonance measurements. On the basis of the latter results, a mechanism was suggested for Li-ion transport inside the PP membrane. The activity of the charcoal cathode was confirmed by Raman and cyclic voltammetry measurements.

© 2024 The Author(s). Published on behalf of The Electrochemical Society by IOP Publishing Limited. This is an open access article distributed under the terms of the Creative Commons Attribution Non-Commercial No Derivatives 4.0 License (CC BY-NC-ND, <http://creativecommons.org/licenses/by-nc-nd/4.0/>), which permits non-commercial reuse, distribution, and reproduction in any medium, provided the original work is not changed in any way and is properly cited. For permission for commercial reuse, please email: permissions@iopublishing.org. [DOI: [10.1149/1945-7111/ad3857](https://doi.org/10.1149/1945-7111/ad3857)]



Manuscript submitted December 17, 2023; revised manuscript received March 17, 2024. Published April 8, 2024.

Supplementary material for this article is available [online](#)

Efficient energy storage and environmental sustainability are of paramount importance in our rapidly developing, energy-consuming world. More than 30% of greenhouse gasses are released by the transportation sector, including aviation, shipping, and residential industries.¹ Therefore, the electrification of existing vehicles will result in a sustainable world. The continuously increasing energy demand requires higher energy densities for various applications such as electric vehicles and satellites.^{2,3} Thus, intensive research is being conducted to develop a new generation of lithium-containing batteries such as lithium–silicon/carbon,⁴ lithium–sulfur,^{5,6} and lithium–air batteries (LABs). The latest, fifth generation of batteries containing lithium is the LAB, which can theoretically provide the highest specific energy with respect to the anode compartment (at an operation voltage of ~ 3 V, it is more than 11000 Wh kg^{-1}).⁷ Furthermore, by using heavy metal-free air cathodes and considering the carbon and water footprints of LABs, LABs are expected to be cheaper and “greener” than current lithium-ion batteries and other lithium battery generations.⁸ At present, no commercial LAB is available in the market. Several difficulties have retarded the commercial introduction of LABs, such as the high reactivity of lithium, the decomposition of organic electrolytes, and the insolubility of the formed lithium oxide.⁹ The lithium anode can react with oxygen and moisture (originating from ambient air); thus, especially for aqueous cells, a special layer is required to prevent these side reactions.¹⁰ Furthermore, special gas diffusion layers (GDLs) are applied at the cathode compartment^{11–13} to prevent the evaporation of solvents and the diffusion of water from the ambient air into the cell while providing appropriate oxygen transport. In addition to the application of GDLs, protective polymer films^{14,15} can be used on the surface of lithium. Furthermore, different lithium-containing alloys¹⁶ or electrolyte compositions¹⁷ have been designed to enhance the corrosion resistance ability and increase the lifetime of lithium anodes in LABs. On the cathode side, the insolubility of different

lithium oxides such as Li_2O_2 , Li_2O , and Li_2O causes the deposition of these salts in the cavities of the cathode, hindering oxygen and lithium-ion transfer, thereby reducing the capacity of the batteries.⁹ Because the discharged products are insoluble in organic solvents, the porosity of the cathode has a significant effect on the deposition of the products formed during discharging.¹⁸ The degradation of the deposited Li oxides (especially that of the Li_2O_2) requires higher energy, leading to higher charging potentials and undesirable side reactions.¹⁹ Some of these reactions are triggered by singlet oxygen formed by the decomposition of Li_2O_2 .¹⁹ The overpotential and side reactions can be minimized by dissolving different additives (such as redox mediators) in the electrolyte.^{20,21} Nevertheless, owing to their high theoretical energy density, extensive studies are in progress to develop safe and long-life LABs suitable for commercial use. Four main types of LABs can be distinguished:⁹ (i) LABs with an aqueous electrolyte,^{22,23} (ii) LABs with a nonaqueous electrolyte,^{24,25} (iii) hybrid cells (an organic solvent at the anode compartment and an aqueous solvent at the cathode compartment),²⁶ and (iv) LABs with a solid electrolyte.^{10,27} The application of solid electrolytes can improve the properties of LABs. For example, metal-oxide-based materials are stable at elevated temperatures and their electrochemical stability is significantly higher than that of organic solvents, providing high (up to 6 V) operation voltage.¹⁹ Nevertheless, the main disadvantage of cells operating with solid electrolytes is their high internal resistance.²⁸

Note that most LABs contain porous carbon, including modified carbon nanotubes,²⁹ Pt/C (Vulcan) cathodes,^{30,31} graphene,^{32,33} and fullerenes.³⁴ However, these cathodes are typically modified (such as N-doped graphene) and/or contain heavy metals, which increase their costs and make them less environmentally friendly.

In this study, a heavy metal-free LAB was constructed using a three-dimensional (3D) printed polypropylene (PP) house with a metal lithium anode and charcoal cathode. The charcoal cathode was successfully used previously in our zinc–air batteries.^{35–37} The electrolyte contained lithium triflate (LiOTf), which is less commonly used than the well-known lithium bis(trifluoromethanesulfonyl)imide (LiTFSI). However, its

²E-mail: keki.sandor@science.unideb.hu

solubility in organic solvents is high, and because of its lower molecular weight, LiOTf has a higher lithium content than LiTFSI. For comparison, three different organic solvents, propylene carbonate (PC), dimethyl sulfoxide (DMSO), and diethylene glycol dimethyl ether (DEGME), were used. The obtained electrolytes were used to soak the cotton texture, and the soaked cotton was then placed on both sides of the PP membrane, combining the benefits of solid cells and the low resistance of the liquid electrolyte. Furthermore, the charcoal cathode is cheap and easily accessible, and when combined with cotton, it is also environmentally friendly.

Experimental

Materials.—Lithium foil (thickness: 0.6 mm) and PP membrane were purchased from Nanografi Nano Technology (Ankara, Turkey) and Xiamen Tmax Battery Equipment Limited, respectively. Charcoal was obtained from Molar Chemicals Ltd (Halásztelek, Hungary), and the diameter of the charcoal particles was calculated by scanning electron microscopy (SEM) (Fig. S1, Supplementary material) using ImageJ software. Supposing ellipse-shaped particles, the major and minor diameters were 13.55 ± 0.08 and 7.55 ± 0.04 μm , respectively. DMSO (99.9%), DEGME (99.5%), PC (99.7%), and LiOTf (96%) were purchased from Merck (Darmstadt, Germany). All chemicals were obtained in anhydrous form and used as received. Cotton canvas with 40 threads/inch (~ 16 threads/cm) was purchased from a haberdashery shop, and its thickness was measured to be 0.30 mm.

Potentiostatic and electrochemical impedance spectroscopy (EIS) measurements.—For the cyclic performance tests, a Biologic SP-150 potentiostat (Seysinnet-Paris, France) equipped with the EC-LAB software package was used. The working potential range was set to 2.0–4.3 V. The charging and discharging currents varied from 1 to 7.5 mA cm^{-2} . The impedance measurements were recorded at 1 mA cm^{-2} from 10 mHz to 500 kHz. Distribution of relaxation time (DRT) calculations were performed using MathWorks Matlab 2022a software. All electrochemical tests were conducted at a constant temperature of 25 °C.

Transmittance measurements.—Transmittance measurements were performed in a rectangular quartz cell (10 × 10 cm) with a 190–2700-nm transparency range using an Agilent Cary 60 spectrophotometer (Agilent, Santa Clara, CA, USA). The inner surface of one side of the cuvette was wetted with the actual solvent, and the PP membrane (45 mm × 9.5 mm, height × width) was placed on the surface. The cuvette was then filled with 3 ml of the solvent. The measurements were performed after 10 min; longer waiting times (2 and 6 h) were also attempted, but no significant difference in the transmittance results was observed.

Raman measurements.—A Horiba LabRam Raman spectrometer was used for the Raman measurements. A 633 nm laser was applied as an excitation source, and the measurement time for each sample was 5 s. The excitation beam was focused onto the sample surface with a 20× objective. The measurement range was 200–2000 cm^{-1} , and a 50% neutral filter was used in all cases.

Scanning electron microscopic (SEM) measurements.—The sizes of the charcoal particles applied were estimated by SEM. SEM images were obtained using a Thermo Fisher Scientific Scios 2 dual-beam scanning electron microscope. The images were taken at an acceleration voltage of 5.00 kV, a beam current of 0.20 nA, a magnification of 650/350, and a dwell time of 100 ns in the secondary electron mode.

Nuclear magnetic resonance (NMR) measurements.—High-field NMR experiments were conducted using a 400-MHz Bruker Avance II spectrometer with a 5-mm inverse broadband probe and a z-gradient coil. The temperature was maintained at 298 K. To avoid

any change in the sample, flame-sealed insert tubes filled with DMSO- d_6 were used. A porous PP separator foil was wrapped around the insert tube, and the corresponding lithium triflate solution was transferred onto it. Air bubbles were removed using vacuum, and the samples were left for a few hours to swell.

After saturation of the samples, ^1H and ^7Li spectra were recorded, and then modified versions of triple-quantum time proportional phase increment (TQTPPI) experiments were conducted. The pulse sequence was the same [$\pi/2(\alpha) - \tau/2 - \pi(\alpha + 90^\circ) - \tau/2 - \pi/2(\alpha + \beta) - \delta - \pi/2(\gamma) - acq(R)$] used by Schepkin et al., where π denotes the 180° RF pulse, τ denotes the incremented delay, α , β , and γ denote the phases of the pulses, δ denotes the mixing time, and R represents the phase of the receiver. It was suggested that the mixing time should be as short as possible; however, we found that a longer mixing time is advantageous for the buildup of the triple-quantum (TQ) signal. A longer mixing time was also required because ^7Li has a longer relaxation time. To stabilize the phases of coherences, EXORCYCLE phase cycling was applied to the phase of the third $\pi/2$ pulse and acq using a $\Delta p = 2$ coherence selection. After this modification, the result was an eight-step phase cycle that stabilized the phases of both single-quantum (SQ) and TQ coherences. An additional improvement was the better suppression of double-quantum coherences. Using this sequence, the separation of the SQ and TQ coherences was possible by performing a second Fourier transformation. The frequency of the coherences was determined by $\Delta\tau$ between steps. The frequencies of SQ and TQ coherences were described by $f(\text{SQ}) = 1/(8 \times \Delta\tau)$ and $f(\text{TQ}) = 3/(8 \times \Delta\tau)$, respectively. TQTPPI experiments were conducted with a mixing time (δ) of 5 ms, 8 scans, and 512 steps. The relaxation delay was 10 s.

PP cell body and electrolytes.—The house of the battery cell was printed from PP (Fiberlogy) using a Prusa i3 MK3S 3D printer (Czech Republic, Prague). The copper collector in the anode compartment was fixed to the PP cell house using epoxy resin. The size of the lithium anode was 10 × 10 × 0.6 mm (length, width, and thickness), resulting 1 cm^2 surface. The cotton cloth (11 × 11 × 0.30 mm) and the PP membrane (11 × 11 × 0.016 mm) were soaked in the electrolyte solution, and 0.25 g of charcoal was mixed with 600 μl of the electrolyte (charcoal mud) 1 h before use. To prepare the cathode, charcoal mud was deposited onto the cotton cloth. The cathode was covered with a PP cap containing holes for air and a copper electron collector. The active area (the sum of the area of the holes) was 0.1 cm^2 , and the mass of activated carbon deposited in this area was 0.7 mg. These data were used to calculate the current density values. The electrolyte was lithium triflate dissolved at 1.0 M in organic solvents, including PC, DMSO, and DEGME. As the last step of battery preparation, the cell was closed with a PP cap containing holes for air and a brass collector for the cathode (Fig. 1).

Results and Discussion

Cycling test.—As discussed above, several forms of carbon cathodes with and without modification have been used in various lithium–air cells.^{29–34} However, to the best of our knowledge, charcoal deposited onto immersed cotton has not yet been tested for this purpose. Our goal was to design a 3D printable Li–air house for the battery and to use the charcoal/cotton layout as the cathode in the presence of LiOTf salt dissolved in three different organic solvents, namely, PC, DMSO, and DEGME. Recently, we successfully used charcoal as the air cathode in a Zn–air secondary battery. Nevertheless, for a Li–air cell, several modifications should be applied. First, on both sides of the PP membrane, cotton textures soaked with a LiOTf electrolyte were placed, providing some additional benefits, including ensuring conductivity inside the cell, preventing any physical damage to the PP membrane during assembly of the cell (for instance by charcoal particles or metal lithium), achieving physical binding for the charcoal between the gaps of the cotton texture, eliminating the application of any

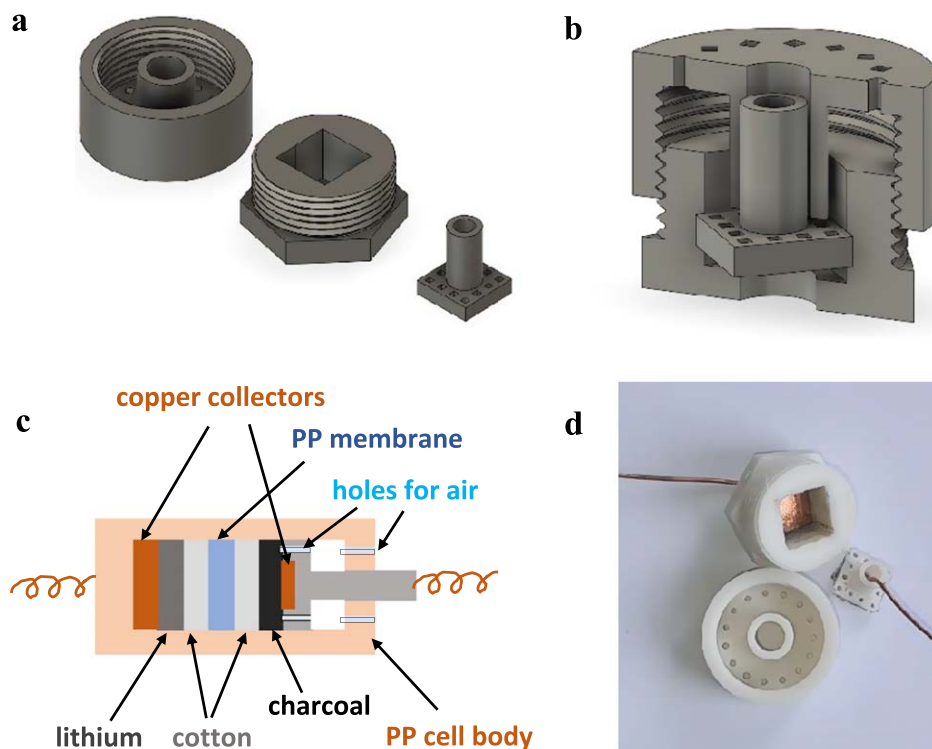


Figure 1. Structure of 3D printed Li-air cell: exploded structure (a), cross-section of the cell body (b), schematic cell structure (c), and photo of the cell (d).

chemical binders and making our cell greener, and preventing/retarding short circuits caused by dendrites, as the shape and type of the dendrites are extensively varied by the shear modulus of medium.³⁸ Finally, the optimal amount of charcoal bound to the cotton texture was determined. It was found that by increasing the thickness of the charcoal layer on the surface of the cotton, the performance of the cell was reduced. The best result was obtained using a charcoal layer as thin as it was possible to make during the handmade preparation containing ~ 0.7 mg charcoal on a 0.1 cm² cotton surface. Using this cell preparation with PC as the solvent, stable operation was observed over 200 cycles, as shown in Fig. 2.

As shown in Fig. 2, the cell operated for over 200 cycles in the presence of the PC solvent; however, previous research has shown that using PC or other cyclic carbonates as solvents, results in

unstable operation.^{39,40} Therefore, better performance is expected with a more electrochemically stable solvent. Thus, our Li-air cell was also tested with the solvents DMSO and DEGME (Fig. 3).

Figures 3a–3c show the cycling test results of the Li-air cell with PC (a), DMSO (b), and DEGME (c) solvents. As evident from Fig. 3, in line with the literature, PC provides the least stable operation compared with the other two electrochemically more stable solvents. Figures 3a–3c also show a significant decrease in the potential in the first 30–50 cycles. To make it more visible, the relative average cell potential (Rel. Avg. E_{we}) was calculated for the first 50 cycles according to Eq. 1.

$$\text{Rel. Avg. } E_{we, i} = \frac{E_{we, \max, i} + E_{we, \min, i}}{2 \times \text{Avg. } E_{we, 1}} \quad [1]$$

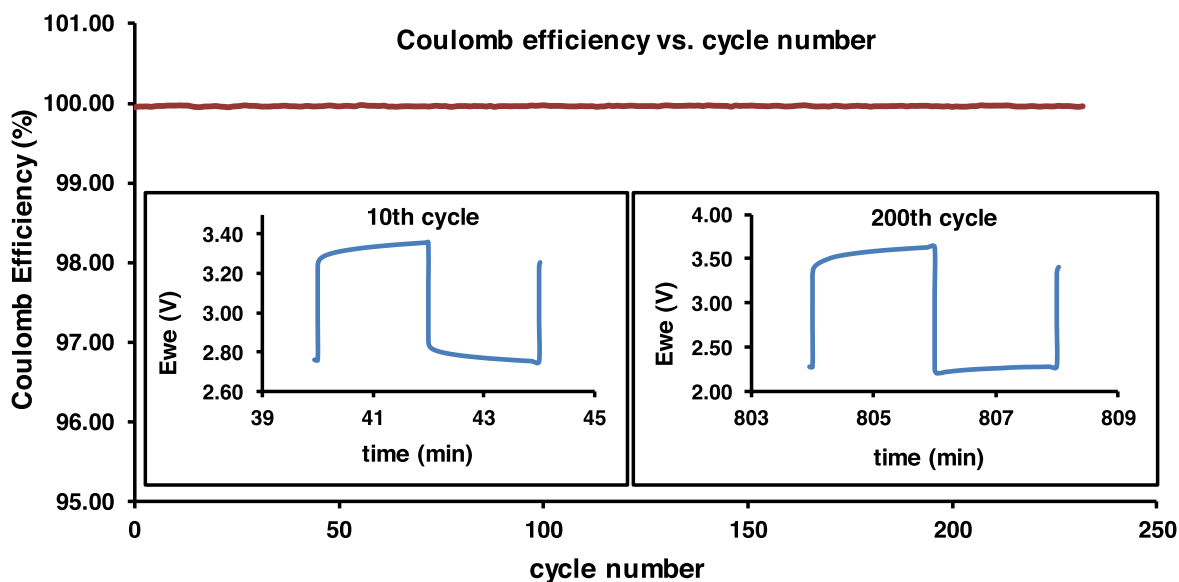


Figure 2. Coulomb efficiency vs cycle number obtained for LAB using a charcoal cathode and 1.0-M LiOTf dissolved in PC. Insets show the 10th and 200th cycles.

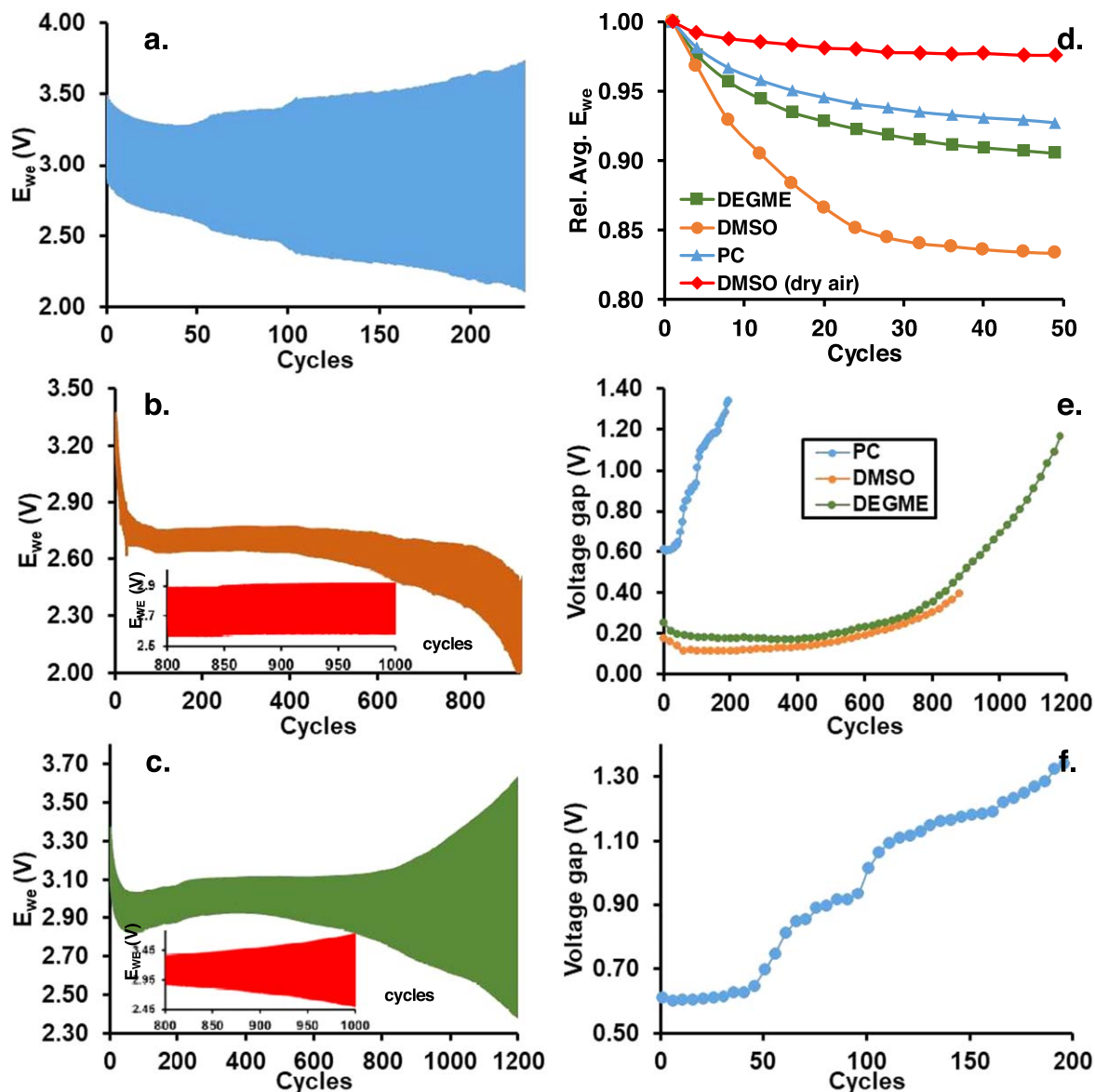


Figure 3. Cycling tests of LABs using PC (a), DMSO (b), and DEGME (c) as solvents (current = 1 mA cm^{-2} ; cycle time = 2 min). (d) and (e) Relative average cell potential and voltage gap against cycles under ambient air, respectively. (f) Enlarged voltage gap data of PC. The insets in (b) and (c) show the results of the cycling test conducted in dry air.

where Rel. Avg. $E_{we,i}$, $E_{we \text{ max},i}$, and $E_{we \text{ min},i}$ denote the relative average potential, the highest potential obtained during the charging period, and the lowest potential obtained during the discharging period for the i th cycle, respectively, and Avg. $E_{we,1}$ denotes the average cell potential for the first cycle calculated as follows: Avg. $E_{we,1} = (E_{we \text{ max},1} + E_{we \text{ min},1})/2$.

As shown in Fig. 3d, the cell potential significantly decreased (by more than 15%) when the DMSO solvent was used in the Li–air cell, whereas, in the cases of PC and DEGME, the potential drop was approximately 5%–8%. Interestingly, the best result (lowest potential drop) was obtained for PC; therefore, the results cannot be interpreted simply using the electrochemical stability of the solvent. Alternatively, it can be explained by the hygroscopic nature of the solvents. Although anhydrous grade solvents were used for the cells in all cases, after beginning cell operation, the solvents can absorb water from the ambient air. Among the three solvents used in this study, DMSO is the most hygroscopic, whereas PC is moderately hygroscopic with limited water solubility at room temperature (8.3 g of water dissolves in 100 g of PC).⁴¹ Furthermore, it has been reported that the partial pressure of water vapor above the

DMSO–water mixture is lower by one order of magnitude than above the PC–water mixture at the same water concentration and temperature⁴² due to the more significant hygroscopic property of DMSO. Unfortunately, no related study has been found for DEGME; however, to estimate its hygroscopic property, data for poly(ethylene glycol) with $M_n = 1540 \text{ Da}$ (PEG1540) were used.⁴³ According to the study reported by Baird et al., at 60% relative humidity,⁴³ the change in the polymer weight was found to be lower than 5 w/w% within 180 days, whereas, for DMSO, it was approximately 50 w/w% within 35 days at 53% humidity.⁴⁴ These findings reveal that dry DMSO is significantly more hygroscopic than dry PEG1540 even though PEG1540 contains -OH end groups, whereas DEGME is an aprotic solvent. Moreover, the dielectric constant of DEGME ($\epsilon = 7.3$) is close to that of PEG400 (11.6)⁴⁵ and significantly lower than that of DMSO (46.7) and PC (64.9), indicating the lower polarity of DEGME. Nevertheless, note that there is no direct correlation between hygroscopicity and dielectric constant, but solvents with low polarity typically exhibit a moderate or low tendency to hygroscopicity or a lower absorption rate for water. Based on these findings, moderate hygroscopic properties can be expected for dry

DEGME compared with dry DMSO. Therefore, it can be assumed that after opening the air cathode and running the battery, DMSO accumulates more water than PC and DEGME during the first 30–50 cycles. Moreover, according to the literature, the adsorption of water occurs on the active sites of activated carbon, and the oxygenated sites play a predominant role in the adsorption process.⁴⁶ Based on these observations, the decreasing potential (Fig. 3d) can be

attributed to the adsorption of water molecules onto the free active sites of the charcoal cathode, thereby reducing the performance and potential of the cell. To prove that the potential drop can be attributed to air humidity, the cell performance was also tested under a dry air atmosphere. As shown in Fig. 3d, the potential drop was minimal for the cell operated with a DMSO-containing electrolyte under dry conditions, whereas, under ambient air, the

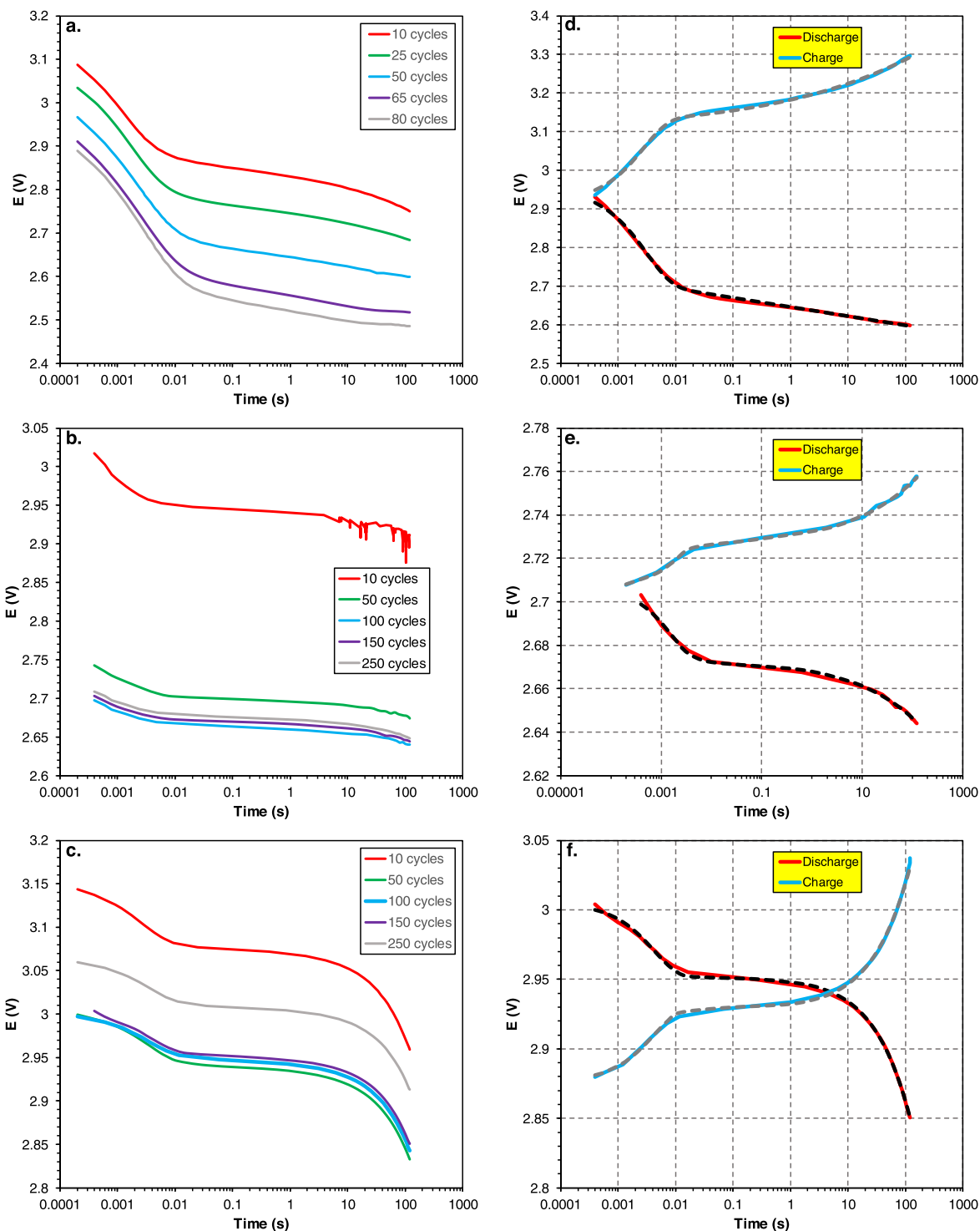


Figure 4. Discharge curves for secondary LABs containing different solvents and using a charcoal cathode at distinct charging/discharging cycles: PC (a), DMSO (b), and DEGME (c). (d)–(f) Show the charge and discharge cyclic tests for secondary LABs containing different solvents: PC (d), DMSO (e), and DEGME (f). The solid lines represent the experimental charge and discharge curves, and the dashed lines represent the fitted data calculated using Eqs. 2 and 3 for the discharging and charging processes, respectively. The experimental curves were obtained in cyclic test numbers of 50 (PC) and 150 (DMSO, DEGME) at a cycle time of 2 min and a constant charge and discharge current of 1 mA cm^{-2} .

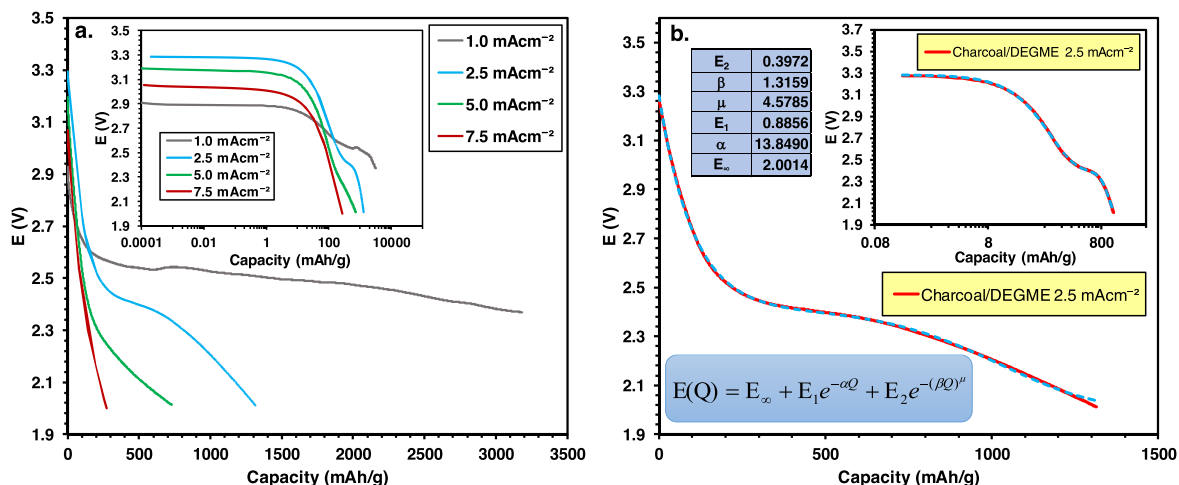


Figure 5. Potential vs capacity curves for secondary LAB containing the solvent DEGME and charcoal cathode at discharge currents of 1, 2.5, 5.0, and 7.5 mA cm⁻² (a). The inset in (a) shows the variation in relative potentials (regarding initial potential as 1) with capacities on logarithmic scales. (b) shows the experimental discharge curve recorded at 2.5 mA cm⁻² (solid line) and the fitted data (dashed line) with the equation used for the fittings (where $Q = I \cdot t$) and the fitted parameters. The inset shows the change in potentials with capacities on logarithmic scales.

Table I. Fitting parameters obtained from Eqs. 2 and 3 for LABs using PC, DMSO, and DEGME solvent. The cycle number is indicated in brackets after the solvent.

Solvent	Parameter	Discharge	Charge
PC (50)	E_2 (V)	4.4478	0.7290
	β (s ⁻¹)	0.0124	2.297×10^{-5}
	μ	0.0063	0.2076
	E_1 (V)	0.2137	0.2015
	α (s ⁻¹)	312.02	361.65
	E_{∞} (V)	0.9647	3.8358
DMSO (150)	E_2 (V)	0.4282	0.1386
	β (s ⁻¹)	4.422×10^{-6}	2.004×10^{-4}
	μ	0.3544	0.3704
	E_1 (V)	0.0334	0.0206
	α (s ⁻¹)	629.80	501.42
	E_{∞} (V)	2.2450	2.8650
DEGME (150)	E_2 (V)	0.7539	0.4369
	β (s ⁻¹)	5.895×10^{-4}	1.412×10^{-3}
	μ	0.7333	0.7487
	E_1 (V)	0.0535	0.0529
	α (s ⁻¹)	238.19	239.66
	E_{∞} (V)	2.1974	3.3659

cell with DMSO exhibited the highest potential drop. Thus, it can be concluded that the hygroscopic solvent accumulates water from the ambient air, and a portion of this water is adsorbed onto the surface of the charcoal cathode. In line with its highest hygroscopicity among the solvents under study, the highest potential drop was observed for DMSO, whereas lower and similar decreasing trends in the potentials were obtained for PC and DEGME. Despite having the highest potential drop, the LAB with DMSO after the first 50 cycles, similar to the cell with DEGME, exhibited stable operation up to ca. 800 cycles (Figs. 3b and 3c). Therefore, it is likely that with the increasing moisture content absorbed from the ambient air, the absorption rate decreases; therefore, it can be assumed that after approximately 50 cycles, the water content in the electrolyte did not vary significantly. Moreover, as shown in Fig. 3e, the voltage gap was lower than 0.4 V after 800 cycles for DMSO and DEGME, whereas, for PC, it started to increase from a value of 0.6 V and reached 1.0 V after 100 cycles. The lower cell performance for PC agrees well with the literature data.^{39,40} Furthermore, the tendency of

variation in the voltage gap is very similar for DMSO and DEGME but different for PC (Fig. 3f). As shown in Fig. 3f, there are two well-separated steps on the voltage gap vs cycle number plot at ca. 50 and 100 cycles. These steps can most probably be attributed to the electrochemical decomposition of PC. The superoxide anion (O_2^-) can undergo further reduction, yielding the hydroperoxide anion (HO_2^-), which induces the decomposition of PC to allyl alcohol ($CH_2=CH-CH_2-OH$) and CO_2 , whereas the initial superoxide anion is re-formed.⁴⁷ Subsequently, the allyl alcohol formed may initiate further side reactions such as chemical corrosion of the metal lithium. In addition, although the voltage gap is slightly lower for DMSO than for DEGME, the variations in the voltage gaps with the number of cycles are very similar. Moreover, after 800 cycles, the behavior of the cells is different (Figs. 3b and 3c). That is, the increase in the voltage gap with the number of cycles is more pronounced in the case of DEGME; however, for DMSO, the LAB reached the 2-V cut-off voltage at approximately 900 cycles. Thus, it can be surmised that in the case of DMSO, the higher moisture content causes chemical corrosion of the lithium anode, resulting in decreased cell potential. Conversely, glycol ethers (such as DEGME) are sensitive to oxidation in the presence of oxygen; thus, oxidative side reactions may occur similarly to PC, yielding higher voltage gaps with an increasing number of cycles. Conducting the tests under dry air conditions, the cell with DMSO exhibited stable operation after 800 cycles (Fig. 3b inset), whereas in the case of DEGME, an increase in the voltage gap was observed after 800 cycles (Fig. 3c inset). This finding indicates that in the latter case, under ambient air conditions, oxidative side reactions occur. Moreover, in a dry air environment, the higher capacity of the cell was tested at a current density of 1 mA cm⁻² and a charging/discharging time of 30 min (Fig. S2, Supplementary material).

To obtain additional information about the performance of the batteries, the individual cycles were also studied. As shown in Figs. 4a–4c, where the discharge curves are shown at distinct cycles for PC (a), DMSO (b), and DEGME (c), there is a significant decrease in the potentials between the 1st and 50th cycles. Consistent with the previous results, the most significant potential drop can be found for DMSO. However, in the case of DMSO and DEGME, after the potential drop, stable operation was obtained over several hundred cycles, resulting in similar discharging voltage curves after 50 cycles, as shown in Figs. 4b and 4c. Conversely, it is also evident from Fig. 4a that because of the low oxidative stability of PC, the potential continuously decreases from cycle to cycle. Interestingly, after a decrease, an increase in the potentials was observed for DEGME, as shown in Fig. 4c at 250 cycles. This

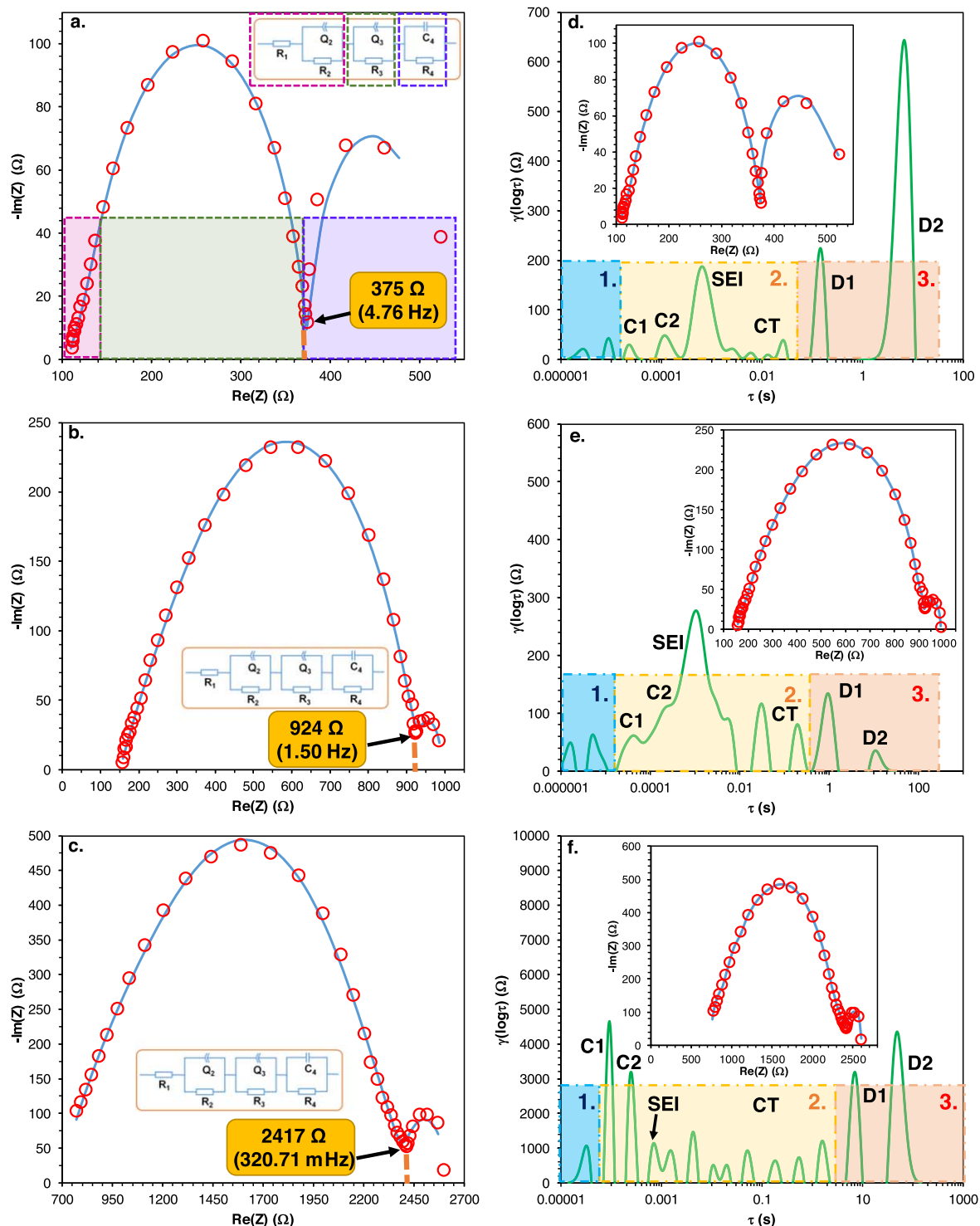


Figure 6. Nyquist plots for secondary LABs containing different solvents recorded at 1 mAcm^{-2} : DEGME (a), DMSO (b), and PC (c). The insets show the fitted equivalent circuit model (ECM), and the characteristic regions described by the ECM are indicated by colors in (a). The symbols represent the experimental data, and the solid lines represent the fitted data. (d)–(f) show the DRT for LABs containing different solvents: DEGME (d), DMSO (e), and PC (f). The insets in (d)–(f) show the curve fitted by DRT. The symbols represent the experimental data, whereas the solid lines represent the fitted data calculated using DRT. $\gamma(\log(\tau))$ denotes the distribution function of relaxation times. The colored regions show typical electrochemical processes: (1) contact, (2) charge transfer and SEI, and (3) diffusion.

finding is in good agreement with previous studies, demonstrating that higher water concentrations result in lower battery performance. Conversely, trace amounts of water can improve cell properties because of the reaction of Li_2O_2 with water.⁴⁸ Therefore, the removal of water by the latter chemical reaction liberates active sites, which can improve the performance of the battery. Similar but

less significant behavior is observed for DMSO in Fig. 4b. It can be rationalized that the absorption of water into the electrolyte and its adsorption onto the charcoal occur simultaneously in the first 50 cycles. Moreover, the adsorption is more significant in DEGME, whereas, in DMSO, both processes occur, most likely, to a similar extent.

Table II. Fitted parameters for Nyquist plots of secondary LABs prepared using different solvents.

Parameter	PC	DMSO	DEGME
R_1 (Ω)	679.1	151.0	105.6
Q_2 ($F \times s^{(a2-1)}$)	0.01236	4.70×10^{-5}	1.80×10^{-4}
a_2	0.8583	0.5097	0.493
R_2 (Ω)	204.2	228.3	37.99
Q_3 ($F \times s^{(a3-1)}$)	1.29×10^{-5}	7.65×10^{-6}	7.34×10^{-6}
a_3	0.5349	0.7836	0.8717
R_3 (Ω)	1343	556.3	232.6
C_4 (F)	2.05×10^{-6}	8.79×10^{-3}	0.02238
R_4 (Ω)	396.9	56.48	141.1

Mathematical modeling of cycles and long-term discharge of LABs.—To mathematically describe the variation in the potential of the LABs during charging/discharging processes, the stretched exponential function model⁴⁹ was used, which has been successfully used for modeling the cycling curves of our Zn–air batteries.³⁶ Figures 4d–4f show the charging/discharging curves at a given number of cycles, along with the fitted curves for PC (d), DMSO (e), and DEGME (f).

As shown in Figs. 4d–4f, Eqs. 2 and 3 adequately describe the cycling curves obtained for our batteries. The fitting parameters are presented in Table I.

For charging,

$$E(t) = E_{\infty} - E_1 e^{-\alpha t} - E_2 e^{-(\beta t)^{\mu}}, \quad [2]$$

for discharging,

$$E(t) = E_{\infty} + E_1 e^{-\alpha t} + E_2 e^{-(\beta t)^{\mu}}, \quad [3]$$

where E_1 and E_2 denote the potential change; α and β denote the rate coefficients of the fast and slow decay, respectively; μ denotes the stretching exponent; E_{∞} denotes the terminal potential.

As shown in Table I, the stretched exponential factor (μ) increases with decreasing solvent polarity and the highest value was found for DEGME (~ 0.75). A similar trend was observed for the Zn–air battery, where a higher μ value was obtained for higher molecular weight-mediated carboxymethyl cellulose with lower functionality (i.e., lower polarity).³⁶ Furthermore, the difference between the μ values obtained for the charging and discharging regimes was lower than 5% in the case of DMSO and DEGME, whereas a significant difference was observed for PC, indicating the low electrochemical stability of PC in LABs.

Because DEGME exhibited the most stable operation in our LABs, long-term discharge studies were also conducted using DEGME. The obtained discharge curves recorded at distinct currents are shown in Fig. 5.

As shown in Fig. 5a, with increasing current density, the capacity decreases and plateaus appear in all cases. However, by compiling all discharge curves in one plot, they are only visible at current densities of 1 and 2.5 mA cm⁻². Thus, to make them visible, the relative potential values (actual potential divided by the initial potential) were plotted against the capacities on logarithmic scales. The highest capacity was obtained at a current density of 1 mA cm⁻². According to Fig. 5b and its inset showing the experimental discharge curve (solid line) and the fitted data (dashed line) at a current density of 2.5 mA cm⁻², the discharge curve can unambiguously be described using the stretched exponential function model. The employed equation and the obtained parameters are shown in Fig. 5b.

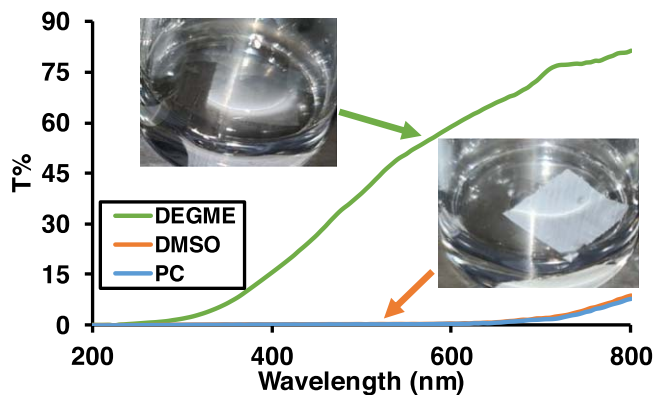


Figure 7. Transmittance of PP membrane recorded at various wavelengths in 1.0-M LiOTf electrolyte containing DEGME, DMSO, and PC solvents. The pictures show the PP membrane in DEGME and DMSO.

Electrochemical impedance spectroscopic (EIS) measurements.—To shed more light on cell operation, impedance measurements were also performed and the DRT was calculated. As shown in Figs. 6a–6c, the resistance increases in the order of DEGME < DMSO < PC. The R_1 values (Table II) correspond to the ohmic resistance of the cell (the real axis intercept of the semicircle at high frequencies), which is mainly caused by the resistance of the PP membrane.⁵⁰ To investigate the behavior of the membrane in the battery, further measurements were performed (see later). Interestingly, the opposite order for the ohmic cell resistance was expected on the basis of the polarity of the solvents, i.e., the resistance decreased in the order of PC (679.1 Ω) > DMSO (151.0 Ω) > DEGME (105.6 Ω). Comparing the R_2 values listed in Table II, which represent the interfacial resistance between the lithium electrode and the electrolyte (the resistance of the passivation film on lithium), the highest value was found for DMSO (228.3 Ω), whereas the lowest value was found for DEGME (37.99 Ω). This finding indicates that the structure of the passivated layer on the lithium anode highly depends on the solvent of the electrolyte. Moreover, as reported by Zhang et al., the thickness of the solid electrolyte interphase (SEI) formed on the surface of lithium decreased from 20 to 10 nm after drying the surface, indicating swelling of the solid electrolyte interface (SEI) on lithium.⁵¹ DEGME is a flexible molecule with three oxygen donor atoms, providing good chelating properties, whereas DMSO and PC are weak complexing agents. Thus, it can be assumed that in the presence of DEGME, a SEI with higher conductivity (lower resistance) was formed because of its flexibility (which provides more modality for incorporation into the SEI lattice) and favorable chelating properties, resulting in a lower R_2 value (Table II).

The R_3 values (Table II) represent the resistance of charge transfer at the electrode/electrolyte interphase. This resistance depends on several factors, such as temperature, coatings, and particles.⁵² The lowest R_3 resistance was found for DEGME (232.6 Ω), and the difference in R_3 values between DMSO (556.3 Ω) and DEGME can be interpreted by the differences in their properties discussed above. However, a significantly higher resistance (1343 Ω) was observed for PC. It is likely that in the case of PC, in addition to its different molecular properties, its electrochemical decomposition remarkably increased the resistance of charge transfer. As discussed above, the oxidative decomposition of PC can occur on the surface of carbon-based cathodes.⁴⁷ The undesirable side reactions can increase the resistance of charge transfer, providing a significantly higher value of R_3 for PC.

The local minima indicated by the arrows reveal the total resistance of the cells. As shown in Fig. 6, the highest resistance (2417 Ω at 320.71 mHz) was determined for the most polar PC, whereas resistance values of 924 Ω (1.50 Hz) and 375 Ω (4.76 Hz) were found for DMSO and DEGME, respectively. The high

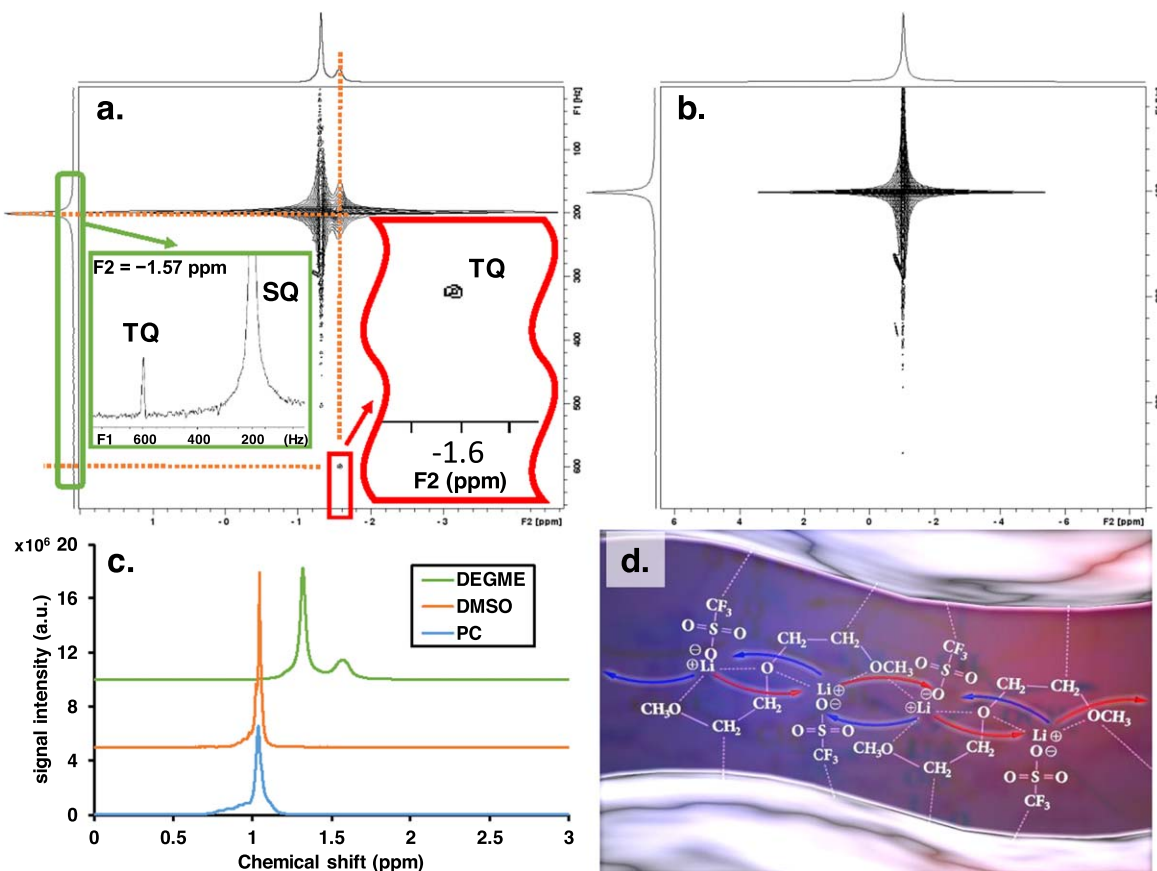


Figure 8. ^7Li -TQTPPI spectrum of the PP membrane in 1.0-M LiOTf electrolyte containing (a) DEGME and (b) DMSO as solvents. The insets in (a) show the TQ signal of lithium in the F1 and F2 dimensions (red) and the SQ and TQ peaks in the F1 dimension (extracted at F2 = -1.57 ppm). ^7Li -NMR spectrum of LiOTf dissolved in DEGME, DMSO, and PC at 1.0-M concentration in the presence of PP membrane (c). (d) shows the suggested mechanism of Li-ion movement in the ion channels of the PP membrane during the charging (blue arrows) and discharging (red arrows) processes.

resistance value for PC agrees with the aforementioned observations. Moving toward lower frequencies after the local minimum, instead of the general shape of the Warburg impedance, an additional semicircle can be observed (Fig. 6). This region of the impedance spectrum is typically attributed to Li-ion diffusion in the electrode and electrolyte. However, it has been shown that an asymmetrical semicircle in the Nyquist plot can be obtained for the cathode at low frequencies if oxygen mass transport (diffusion) is the dominant factor in cell operation, and it can be negligibly small at a low cathode thickness or low oxygen concentration.⁵³ In our LAB configuration, the thickness of the charcoal cathode can be regarded as constant; thus, the presence of a second semicircle at low frequencies can be interpreted by dominant oxygen mass transport at the surface of the charcoal cathode, which can be described by Gerischer impedance.⁵³ Moreover, a second semicircle at low frequencies was observed for all three solvents (Figs. 6a–6c), indicating an appropriately high oxygen concentration at the cathode. In addition, the asymmetrical shape of this semicircle observed for DEGME (Fig. 6a) is most probably due to the superimposition of additional physical and electrochemical processes, including the diffusion of Li ions. The R_4 values found in Table II may describe the diffusion processes. The lowest R_4 resistance (56.48 Ω) for DMSO suggests better Li-ion diffusion than that in a less polar DEGME electrolyte (141.1 Ω), whereas the higher R_4 value (396.9 Ω) for PC can be attributed to undesired electrochemical side reactions. Furthermore, as presented in Table II, lower C_4 capacitance was found for higher solvent polarity, and the C_4 value obtained for PC ($2.05 \cdot 10^{-6}$ F) is in the order of typical capacitance values published in the literature for electrochemical double layers.⁵⁴

On the basis of impedance spectroscopy, DRT analysis was performed using Matlab software^{55,56} to gain deeper insight into the contributions of different processes. DRT is an effective method for identifying the different electrochemical processes involved in the impedance spectra. The time constants (τ) of processes increase as follows: the contact process < the process of passive films on electrodes < the charge transfer process < the diffusion processes on electrodes.⁵⁷ Typically, diffusion processes are not informative in DRT because the anode and cathode processes cannot be distinguished. As shown in Figs. 6d–6f, the two peaks that appeared at high τ values (D1 and D2, in region 3) can be attributed to the diffusion processes on the anode and cathode surfaces. Furthermore, a positive shift in the time constants of these peaks from DEGME (Fig. 6d) to PC (Fig. 6f) can be seen, and the intensity ratio of these two peaks also changes significantly. Interestingly, based on the relative intensities, peak D2 is more dominant if the relative intensity of the second semicircle (at the imaginary axis) in the impedance spectrum is higher. Moreover, the presence of two peaks in the diffusion region indicates two distinct diffusion regimes, possibly for Li ions and oxygen molecules (or Li species such as peroxide ions). In region 2, at higher relaxation times ($\tau > 0.001$ s), DRT peaks attributed to the charge transfer processes of the cathode and anode are present. As shown in Fig. 6f, several peaks are visible in this region for PC, which may be ascribed to the chemical/electrochemical side processes. The highest intensity peaks in this region (Figs. 6d and 6e) correspond to lithium transport through the SEI layer.⁵⁸ Interestingly, the intensity of the SEI peak was significantly lower for PC (Fig. 6f). C1 and C2 can be attributed to cathodic processes and/or liquid films formed on the surface of the cotton fibers. The DRT peaks referring to contact processes such as

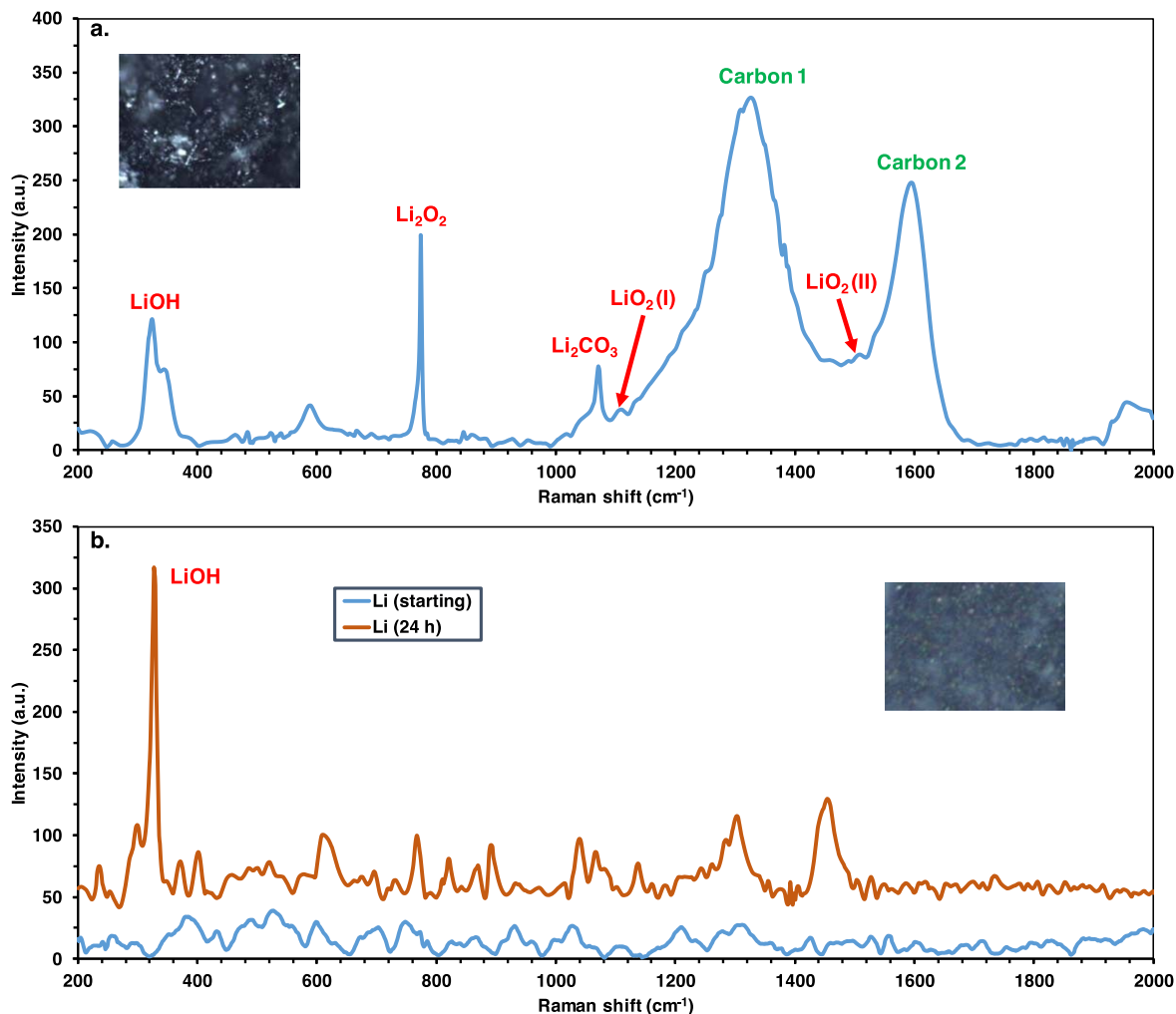


Figure 9. Intensity vs Raman shifts for charcoal cathode (a) and lithium anode (b) obtained after a 24-h cyclic test at discharge. Insets show pictures of the electrodes.

those that occur between the electrode and current collector occurred at low τ values (high frequencies) in Region 1.⁵⁷

Behavior of the PP membrane in LAB.—As discussed above, the lowest ohmic resistance was obtained for the LAB with a less polar DEGME. It was found that during cell preparation by the addition of DEGME to the white PP membrane, its transparency significantly increased, whereas no similar phenomenon was observed for DMSO and PC (Fig. 7).

Figure 7 shows that a significant transmittance value is measured for the PP membrane in DEGME in the visible wavelength region, whereas it is negligible for DMSO and PC.

On the basis of these observations, it was rationalized that better swelling of the nonpolar PP membrane could occur in DEGME of low polarity, aiding the permeation of LiOTf salt into the membrane and thus forming Li-ion channels. To support this theory and gain better insight into the membrane processes, NMR measurements, including TQTPPI with the pulse sequence introduced by Schepkin et al.,⁵⁹ were performed. Figures 8a and 8c show the ⁷Li-TQTPPI and ⁷Li-NMR spectra of the PP membrane in the electrolyte solution containing LiOTf salt dissolved in DEGME at a concentration of 1.0 M, respectively. As shown in Fig. 8c, in DEGME, two states of lithium ions were detected, whereas, in DMSO and PC, only one peak was observed. The intensive peak in the spectrum recorded in DEGME (Fig. 8c) corresponds to Li ions in the bulk electrolyte phase; however, the second peak can be attributed to Li ions incorporated into the PP membrane. Furthermore, in the ⁷Li-TQTPPI spectrum, an additional

TQ signal was detected in addition to the SQ signal, revealing a third state of lithium (Fig. 8a insets). The detection of the TQ signal of the lithium ion can be interpreted by the interaction between the lithium ion incorporated into the PP membrane and that adsorbed onto the PP membrane surface. Similar TQ signals and interactions were not detected in DMSO (Fig. 8b or PC). Thus, the NMR results show lithium ions with three different states in the PP membrane–DEGME–LiOTf system: the lithium ion in the bulk electrolyte, the lithium ion adsorbed onto the surface of the PP membrane, and the lithium ion inside the PP membrane (the incorporated lithium ion). Note that the permeation of lithium ions into the PP membrane is also possible in the cases of DMSO and PC solvents (as our LAB functioned with these solvents). Moreover, this process seems to be less significant because NMR failed to detect it. On the basis of these findings, it can be concluded that in the electrolyte containing DEGME, a more pronounced swelling process of the PP membrane occurs, yielding additional ion channels through the membrane and resulting in lower ohmic resistance of the LAB. On the basis of these results, a mechanism was suggested for Li-ion transport through the PP membrane (Fig. 8d). Accordingly, as shown in Fig. 8d, there is an ion channel in the PP membrane: the nonpolar moieties of DEGME and LiOTf are coordinated to the PP wall, whereas the polar moieties, including lithium, are arranged around the center of the channel, far away from the PP wall. During the charging and discharging processes, because of the presence of oxygen donor atoms, conduction occurs by Li-ion hopping (as indicated by the blue and red arrows in Fig. 8d), which is a well-known phenomenon in Li-ion batteries.⁶⁰

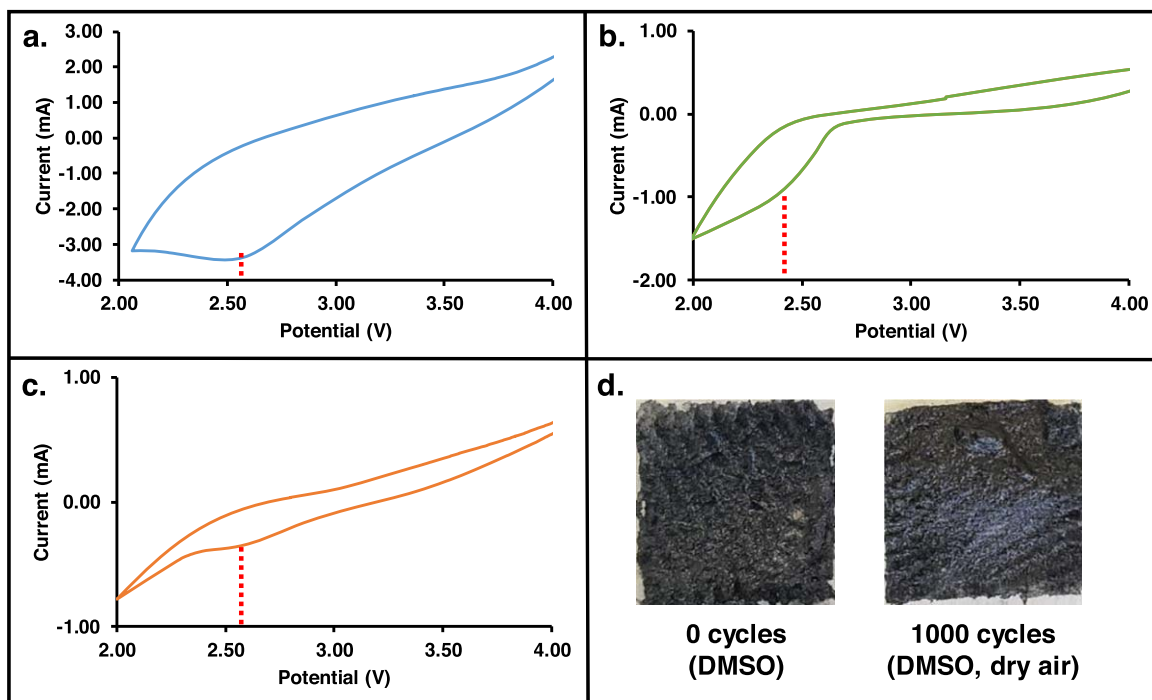
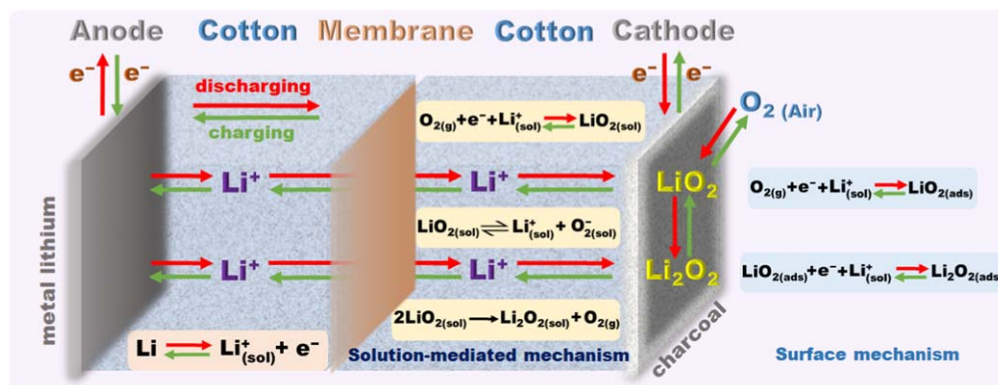


Figure 10. CVs of LAB recorded in ambient air (a) and dry oxygen (b), (c) using 1.0-M LiOTf dissolved in DEGME (a), (b) and DMSO (c) as electrolytes. The scan rate was 5 mV s^{-1} in all cases. (d) Charcoal cathode after 0 and 1000 cycles using DMSO-containing electrolyte.



Scheme 1. Proposed mechanism for LAB operation.

Raman spectroscopy and cyclic voltammetry.—To study the products formed on the charcoal cathode and lithium anode during the LAB operation, Raman measurements were performed. Peaks in the Raman spectra were identified using reference data.^{61–63} As shown in Fig. 9, LiOH was detected at 327 cm^{-1} on the cathode (Fig. 9a) and anode (Fig. 9b) after 24 h of battery operation. Note that in the case of lithium during the Raman measurements, lithium was kept under a thin hexane layer to prevent it from reacting with the components of the ambient air.

Several peaks were identified in the Raman spectrum of the cathode. First, the two main peaks in Fig. 9a correspond to the typical carbon peaks detected at 1332 and 1600 cm^{-1} . Furthermore, a peak was observed at 1075 cm^{-1} , and the shoulder of this peak was found at 1040 cm^{-1} . These Raman shifts correspond to Li_2CO_3 .⁶³ Moreover, Li_2O_2 (at 778 cm^{-1}) and typical shifts of LiO_2 (at 1117 and 1509 cm^{-1}) were also observed in the Raman spectrum of the cathode. The presence of these Li oxides proves the activity of the cathode.

The activity of charcoal as the cathode was also recognized in the cyclic voltammogram (CV) (Fig. 10).

As shown in Fig. 10a, a reduction peak occurred at approximately 2.5 V in the DEGME-containing electrolyte, indicating the activity of the cathode. Similar results have been reported for graphene nanosheets;⁶⁴ however, nitrogen doping had to be achieved to make the reduction peak in CV more visible; whereas, in our cell, unmodified charcoal had been used. In the CV measurements in dry oxygen using DEGME (Fig. 10b) and DMSO (Fig. 10c) as solvents, a slight shift of the cathodic peak was found at lower potentials for DEGME, which can be attributed to its oxidative sensitivity. Nevertheless, the physical stability of the cathode was excellent in all three solvents applied, as shown in Fig. 10d, which shows no significant difference in the appearance of the charcoal cathode after 0 and 1000 cycles using the DMSO solvent.

On the basis of the Raman spectroscopic and cyclic voltammetric results, the mechanism shown in Scheme 1 was proposed. According to Scheme 1, during the discharging process, the metal lithium dissolves in the form of solvated lithium ions ($\text{Li}^+_{(\text{sol})}$), whereas LiO_2 forms ($\text{LiO}_{2(\text{ads})}$) on the surface of the charcoal cathode by oxygen reduction. Subsequently, further reduction of LiO_2 occurs, producing Li_2O_2 (a surface mechanism). However, according to the

literature,²⁵ the solution-mediated mechanism can be significant in the case of electrolytes containing polar solvents (such as DMSO). According to this mechanism, a significant amount of LiO₂ can dissolve in the electrolyte (LiO_{2(sol)}) to yield Li₂O₂ and oxygen by disproportionation.

Conclusions

In this study, LABs were designed using a charcoal cathode, metal lithium anode, and PP membrane. Furthermore, the cotton texture was soaked in an organic electrolyte containing lithium. The batteries were investigated using three different organic solvents: PC, DMSO, and DEGME. It was demonstrated by long-term performance tests that charcoal deposited onto cotton texture is a suitable cathode for LABs. Furthermore, stable cell operation with practically 100% coulombic efficiency was found at more than 800 cycles in the cases of DMSO and DEGME, whereas the same was obtained at only 200 cycles for PC because of its low electrochemical stability in LABs under ambient air. It was also highlighted that using dry air, battery operation can be considerably prolonged. Furthermore, the obtained cycles and long-term discharge curves were successfully described mathematically using the stretched exponential model. To gain a deeper insight into battery operation, EIS measurements were performed, and DRTs were calculated and evaluated. The highest ohmic resistance of the battery was found for PC, whereas the lowest value was obtained for DEGME. The swelling properties of the PP membrane were studied by transmittance and NMR measurements, which confirmed better swelling of the PP membrane in the less polar DEGME. The ⁷Li-TQTPPI measurements showed three lithium states in the presence of the PP membrane using DEGME. On the basis of these findings, a mechanism was suggested for the transport of Li ions through the PP membrane. In the DRT spectra, peaks due to diffusion, charge transfer, and SEI processes were identified, and the activity of charcoal as the cathode was also proved by Raman and cyclic voltammetry measurements.

Acknowledgments

Project no. RRF-2.3.1–21–2022–00009, titled National Laboratory for Renewable Energy, was implemented with the support provided by the Recovery and Resilience Facility of the European Union within the framework of Programme Széchenyi Plan Plus. Furthermore, the work was supported by Hungarian National Scientific Research Fund Grant No. NKFIH K-131989. Special thanks to Victor D. Schepkin for his help in implementing the TQTPPI method and to Gergő Róth for the DRT calculations.

ORCID

Sándor Kéki  <https://orcid.org/0000-0002-5274-6117>

References

- Z. Liu, Z. Deng, S. Davis, and P. Ciais, *Nat Rev Earth Environ*, **4**, 205 (2023).
- M. M. Thackeray, C. Wolverton, and E. D. Isaacs, *Energy Environ. Sci.*, **5**, 7854 (2012).
- S. S. Zhang, *J. Power Sources*, **164**, 351 (2007).
- Y. Qiao, S. Yang, Z. Ma, Y. Yang, X. Hong, and Z. Fu, *Nano Res.*, **16**, 8394 (2023).
- L. Kong, H.-J. Peng, J.-Q. Huang, and Q. Zhang, *Nano Res.*, **10**, 4027 (2017).
- Z. Xiong, G. Zhang, Y. Ding, J. You, and S. Cheng, *Int. J. Electrochem. Sci.*, **18**, 100215 (2023).
- J. P. Zheng, R. Y. Liang, M. Hendrickson, and E. J. Plichta, *J. Electrochem. Soc.*, **155**, A432 (2008).
- L. Wang, J. Hu, Y. Yu, K. Huang, and Y. Hu, *J. Cleaner Prod.*, **276**, 124244 (2020).
- A. Suryatna et al., X. Liu, (ed.) *J. Chem.*, **2022**, 1 (2022).
- P. Chen, F. Bai, J. W. Deng, B. Liu, and T. Zhang, *Front. Chem.*, **10**, 1035691 (2022).
- J. H. Kang et al., *ACS Nano*, **14**, 14549 (2020).
- A. Jaradat et al., *Small*, **17**, 2102072 (2021).
- L. Wang, J. Pan, Y. Zhang, X. Cheng, L. Liu, and H. Peng, *Adv. Mater.*, **30**, 1704378 (2018).
- T. Liu et al., *Angew. Chem. Int. Ed. Engl.*, **58**, 18240 (2019).
- Y. Yu et al., *Energy Storage Mater.*, **18**, 382 (2019).
- X. Liang et al., *Nat. Energy*, **2**, 1 (2017).
- Y. Yu et al., *Energy Environ. Sci.*, **13**, 3075 (2020).
- A. Zahoor et al., *ACS Sustainable Chem. Eng.*, **7**, 14288 (2019).
- H. Kim, W.-J. Kwak, H.-G. Jung, and Y.-K. Sun, *J. Mater. Chem. A*, **8**, 5622 (2020).
- W.-J. Kwak et al., *Mater. Horiz.*, **7**, 214 (2020).
- Y. Ko, H. Park, B. Kim, J. S. Kim, and K. Kang, *TRECHEM*, **1**, 349 (2019).
- Graduate School of Engineering, Mie University, Tsu, Mie, 514-8507, Japan et al., *JEPT*, **4**, 1 (2022).
- P. He, Y. Wang, and H. Zhou, *Chem. Commun.*, **47**, 10701 (2011).
- J. Zhang et al., *Nat. Commun.*, **10**, 602 (2019).
- T. Liu, J. P. Vivek, E. W. Zhao, J. Lei, N. Garcia-Araez, and C. P. Grey, *Chem. Rev.*, **120**, 6558 (2020).
- P. He, T. Zhang, J. Jiang, and H. Zhou, *J. Phys. Chem. Lett.*, **7**, 1267 (2016).
- Y. Liu et al., *ACS Appl. Mater. Interfaces*, **7**, 17307 (2015).
- L. Li and A. Manthiram, *J. Mater. Chem. A*, **1**, 5121 (2013).
- Y. Li et al., *Electrochem. Commun.*, **13**, 668 (2011).
- D. Su, H.-S. Kim, W.-S. Kim, and G. Wang, *J. Power Sources*, **244**, 488 (2013).
- S. S. H. Zaidi et al., *Nano Res. Energy*, **2**, e9120055 (2023).
- W. G. Chong et al., *Nanoscale*, **11**, 6334 (2019).
- S. S. H. Zaidi, S. Sigdel, C. M. Sorensen, G. Kwon, and X. Li, *J. Electrochem. Energy Convers. Storage*, **20**, 020907 (2023).
- N. Bharadwaj, A. S. Nair, S. Das, and B. Pathak, *ACS Appl. Energy Mater.*, **5**, 3380 (2022).
- T. Nagy et al., *Electrochim. Acta*, **368**, 137592 (2021).
- T. Nagy et al., *J. Energy Storage*, **49**, 104173 (2022).
- T. Nagy et al., *Batteries*, **8**, 212 (2022).
- L. Frenck, G. K. Sethi, J. A. Maslyn, and N. P. Balsara, *Front. Energy Res.*, **7**, 115 (2019).
- S. A. Freunberger et al., *J. Am. Chem. Soc.*, **133**, 8040 (2011).
- L. Grande et al., *Adv. Mater.*, **27**, 784 (2015).
- T. Fujinaga and K. Izutsu, *Pure Appl. Chem.*, **27**, 273 (1971).
- S. Y. Lam and R. L. Benoit, *Can. J. Chem.*, **52**, 718 (1974).
- J. A. Baird, R. Olayo-Valles, C. Rinaldi, and L. S. Taylor, *J. Pharm. Sci.*, **99**, 154 (2010).
- Gaylord Chemical, <https://gaylordchemical.com/products/literature/physical-properties/>.
- K. Arnold, A. Herrmann, L. Pratsch, and K. Gawrisch, *Biochim. Biophys. Acta*, **815**, 515 (1985).
- C. L. McCallum, T. J. Bandosz, S. C. McGrother, E. A. Müller, and K. E. Gubbins, *Langmuir*, **15**, 533 (1999).
- V. S. Bryantsev and M. Blanco, *J. Phys. Chem. Lett.*, **2**, 379 (2011).
- X. Zhang et al., *Energy & Environ. Materials*, **1**, 61 (2018).
- D. C. Johnston, *Phys. Rev. B*, **74**, 184430 (2006).
- T. Zhang et al., *J. Electrochem. Soc.*, **155**, A965 (2008).
- Z. Zhang et al., *Science*, **375**, 66 (2022).
- W. Choi, H.-C. Shin, J. M. Kim, J.-Y. Choi, and W.-S. Yoon, *J. Electrochem. Sci. Technol.*, **11**, 1 (2020).
- M. Mehta, G. Mixon, J. P. Zheng, and P. Andrei, *J. Electrochem. Soc.*, **160**, A2033 (2013).
- R. S. Lillard and B. A. Pint, (2020), in *Comprehensive Nuclear Materials*. 1 (Elsevier, Amsterdam), <https://linkinghub.elsevier.com/retrieve/pii/B9780128035818117618>.
- T. H. Wan, M. Saccoccio, C. Chen, and F. Ciucci, *Electrochim. Acta*, **184**, 483 (2015).
- A. Maradesa, B. Py, T. H. Wan, M. B. Effat, and F. Ciucci, *J. Electrochem. Soc.*, **170**, 030502 (2023).
- J. Zhu et al., *IEEE Trans. Transp. Electrification*, **7**, 410 (2021).
- T. Wang, X. Pan, J. Chen, and Y. Chen, *J. Phys. Chem. Lett.*, **12**, 4799 (2021).
- V. D. Schepkin, A. Neubauer, A. M. Nagel, and T. F. Budinger, *J. Magn. Reson.*, **277**, 162 (2017).
- K. Dokko et al., *J. Phys. Chem. B*, **122**, 10736 (2018).
- F. S. Gittleston et al., *Chem. Electro. Chem.*, **2**, 1446 (2015).
- A. Halder et al., *ACS Energy Lett.*, **3**, 1105 (2018).
- D. Zhai et al., *J. Phys. Chem. Lett.*, **5**, 2705 (2014).
- Y. Li et al., *Electrochem. Commun.*, **18**, 12 (2012).